Numerical modeling of cave propagation and breakthrough timing: A back-analysis at New Afton mine

C. Cancino[a], M. Fuenzalida[a] and C. Kamp[b]
[a]*Itasca Minneapolis, USA*
[b]*New Gold Inc., Canada*

ABSTRACT

New Afton Mine located 10 km outside Kamloops, Canada, started operating two separate caves, the West and East Caves (Lift 1), with production levels located approximately 600 m below the surface. The new B3 panel is located 160 m below and immediately to the west of Lift 1. Production at the B3 panel started mid-2021. A critical component of effective production for the B3 panel is successful cave propagation and breakthrough timing with Lift 1. Metallic and Optical Time Domain Reflectometry (MTDR and OTDR respectively) sensors were installed to assess cave initiation and propagation at B3. Also, seismicity was recorded, and cave tracker beacons were installed to assess flow behavior inside the muckpile. In 2022, a series of calibration stages over several months was completed to then provide refined numerical projections of the mobilized and yielded zones. The calibration of the B3 Cave was conducted using a hybrid modeling approach (*FLAC3D-MassFlow*) to simulate both the draw/flow and caving propagation to determine abutment stresses and cave loads induced on the extraction level as material was drawn. The model was calibrated with field data to better estimate cave propagation and the breakthrough timing with Lift 1. A proper prediction of the connection time was necessary to abandon the production level still active underneath Lift 1. This paper discusses the significance of using a strain-softening model (*IMASS*) with the ability to capture the correct mechanics of rock mass frictional strength mobilization, and the use of a hybrid *FLAC3D-MassFlow* modeling approach for a precise back-analysis of cave performance.

1 INTRODUCTION

New Afton is a block caving mine located 10 km outside Kamloops, British Columbia, Canada. The mine was developed between 2007 and 2012, and mill production commenced in 2012. A schematic view of the New Afton Mine is illustrated in Figure 1. Initial Lift 1 mining comprised production from adjacent West and East Caves from 2011 and Q1 2022. Subsequent B3 mining was initiated in mid-2021 and remains active, located beneath Lift 1 West Cave and to the west of the Afton pit (~760 m below the surface). The B3 Cave introduces new challenges and opportunities, notably the critical synchronization of cave propagation and breakthrough timing with Lift 1.

This paper focuses on the B3 Cave stages of initiation, propagation, and breakthrough of Lift 1. The use of Metallic and Optical Time Domain Reflectometry (MTDR and OTDR respectively) cables, seismic source locations, Geo4Sight, passive tomography, and cave tracker beacons serves as evidence to the mine's commitment to a comprehensive understanding of cave initiation, propagation, and flow dynamics within the muckpile.

Adopting a hybrid modeling approach, integrating *FLAC3D* (Itasca, 2023a) and *MassFlow* (Itasca, 2023b) models, a numerical calibration aimed to not only simulate drawdown of caved material but also cave propagation to determine abutment stresses and cave loads induced on the extraction level as material was drawn. Calibrated against on-site data, this model facilitates predictions of cave propagation and breakthrough timing with Lift

1, guiding decisions related to the strategic abandonment of active production levels (West Cave EXL), haulage and vent galleries beneath Lift 1 depicted in Figure 2.

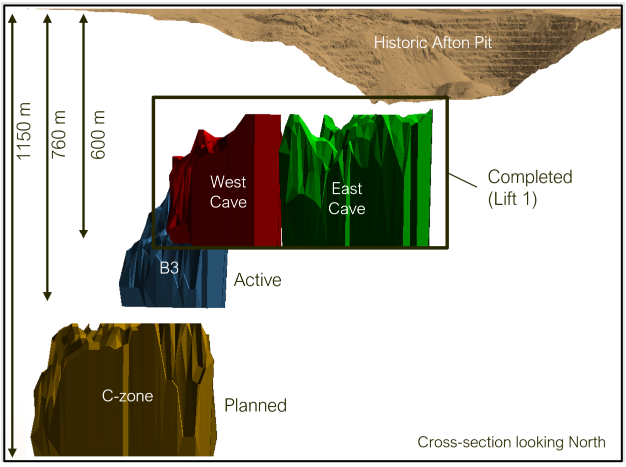

Figure 1 New Afton Mine layout.

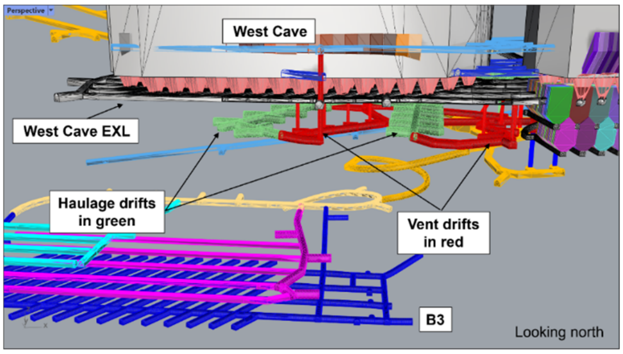

Figure 2 Location of haulage and vent drifts underneath the West Cave relative to B3.

2 NUMERICAL METHOD FOR ANALYSIS OF CAVING

A mine-scale *FLAC3D-MassFlow* hybrid model was constructed for caving analysis at New Afton Mine. This approach can explicitly simulate the air gap formation and more complex mechanisms such as rilling within the mobilized zone and, therefore, is able to provide a more reliable prediction of caveability, cave propagation, timing of breakthrough, and subsidence impact on surface infrastructure. In addition, the model can provide insights on the effect of cave-induced stresses and rock mass deformation on the performance of underground infrastructure. The flow component of the coupled model (*FLAC3D-MassFlow*) can provide information regarding dilution and recovery as well as fragmentation and fines migration.

2.1 Modeling Approach

The hybrid *FLAC3D-MassFlow* approach simulates the caving process by explicitly modeling each isolated movement zone (IMZ) derived from *MassFlow* in *FLAC3D* to determine the yielded zone, cave back, and air gap associated with mass drawn as introduced by Fuenzalida et al. (2018) in the hybrid *FLAC3D-REBOP* approach. After one cycle of extraction, *MassFlow* reports the location of the movement zones and the presence of air (if present) to the continuum *FLAC3D* model (Figure 3). *FLAC3D* solves stresses associated with the presence of these zones and estimates the yielded zone surrounding the cave. *FLAC3D* then informs *MassFlow* which zones (initially inactive) could now be mobilized. The procedure is repeated until the draw schedule, used as an input in *MassFlow*, is completed.

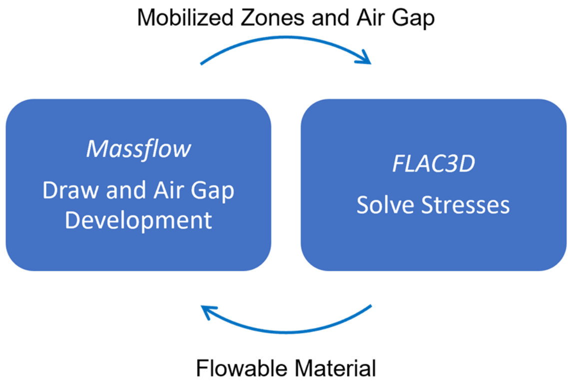

Figure 3 Conceptual scheme of the hybrid *FLAC3D-MassFlow* approach (after Fuenzalida et al. 2018).

2.2 Constitutive Model

As introduced by Pierce (2013), a numerical model that represents the caving process must account for the progressive failure and disintegration of the rock mass from an intact/jointed elastic condition to a fully broken material (bulked). In this complex process, creation of the cave results in deformation and stress redistribution of the rock mass above the undercut, failure of the rock mass in advance of the cave with an associated progressive reduction in strength from peak to residual levels, and dilation, bulking, fragmentation, and mobilization of the cave material.

This overall process of loading the rock mass to its peak strength, followed by post-peak reduction in strength to some residual level with increasing strain, is often termed as a strain-softening process and is the result of strain-dependent material properties.

The Itasca Model for Advanced Strain Softening (*IMASS*) constitutive model (Ghazvinian et al., 2020) was used in this study. *IMASS* is a strain-softening model for simulation of rock mass response to mining. This model contains a two-stage softening behavior as depicted in Figure 4. The first residual envelope (blue line) represents the post-peak strength. At this point, the rock mass is assumed to have undergone fracturing, but the resulting rock fragments are still fully interlocked. The second residual envelope (green line) represents the ultimate residual strength at the point of maximum bulking. At this point, the degree of rock fragment interlock is at its minimum, and the porosity is maximized.

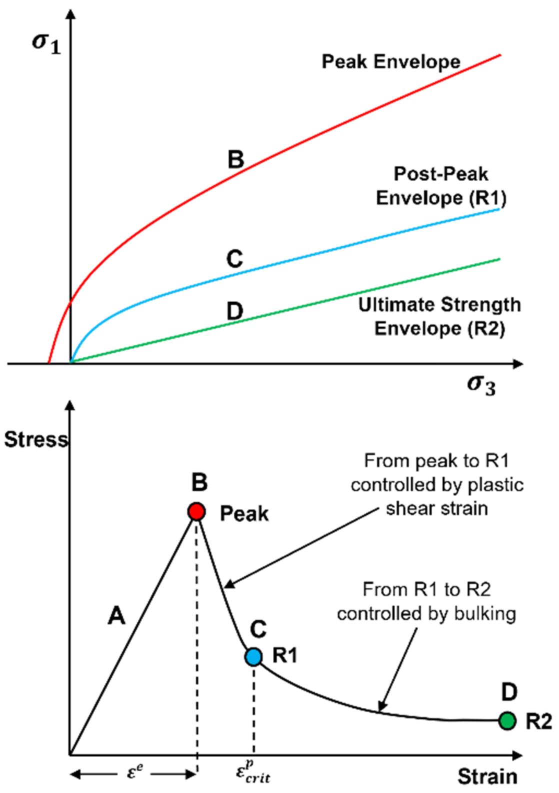

Figure 4 Yield surfaces and material response for *IMASS* model (after Ghazvinian et al., 2020).

2.3 *MassFlow*

MassFlow (Itasca, 2023b) and its predecessor *REBOP* (Itasca, 2019) were developed based on physical and numerical modeling as a tool for rapid simulation of material flow within block, panel, and sublevel caves (Pierce, 2010). *MassFlow* models flow by tracking the growth of the isolated movements zones (IMZ) and the internal material movement associated with draw. Figure 5 illustrates the IMZ growth and material movement with incremental draw.

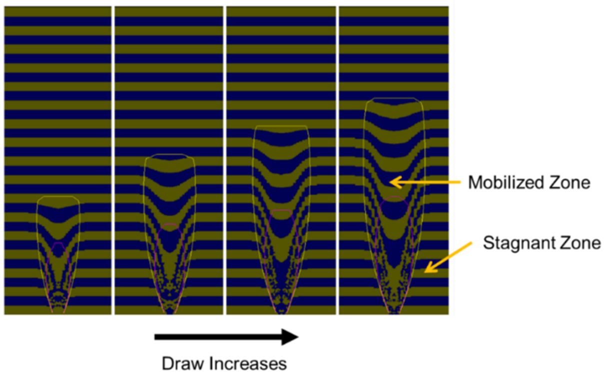

Figure 5 Draw zone growth in *REBOP* with incremental draw (Pierce, 2010).

MassFlow requires three inputs: 1) a block model containing information on primary fragment size and porosity; 2) drawpoint coordinates; and 3) a draw schedule.

2.4 *Conceptual model of caving and definition of fracture limit*

A conceptual model of a propagating cave has previously been developed by Duplancic and Brady (1999) through seismic investigations and underground instrumentation at the Northparkes Mine in Australia. The conceptual model includes four main behavioral regions that are illustrated in Figure 6.

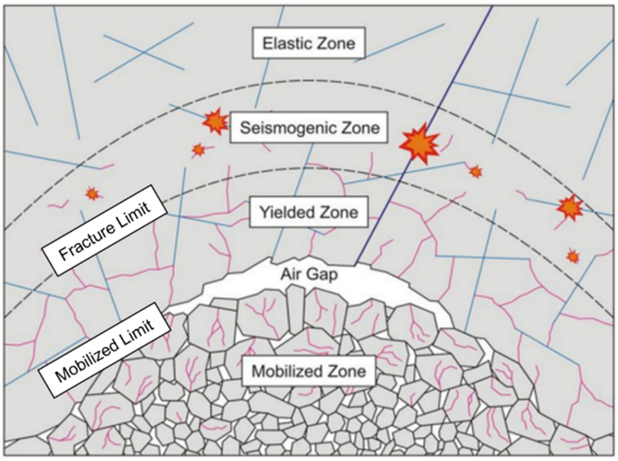

Figure 6 Schematic outlining the caving zones modified with the Fracture Limit and Mobilized Limit from Duplancic and Brady (1999).

The elastic zone represents the host rock mass around the caving region that behaves mainly elastically and has properties consistent with an "undamaged" rock mass.

The seismogenic zone represents the region where microseismic activity is concentrated due to slip along pre-existing discontinuities and the initiation of new fractures.

The rock mass in the yielded zone is fractured and has lost some or all its cohesive strength and provides minimal support to the overlying rock mass. A rock mass within the yielded zone is subject to significant damage, i.e., open holes may be cut-off, TDR clipping is expected, and cracking is observable in infrastructure. Stress components within this region are typically low in magnitude due to lack of confinement.

Air gap can exist if the overlying rock mass within the yielded zone retains some level of cohesive and/or tensile strength, and the cave propagation rate is lower relative to the draw rate.

Finally, the mobilized zone gives an estimate of the portion of the orebody that has moved in response to the production draw and may be recoverable through the drawpoints.

2.4.1 Definition of mobilized limit

Although the specific location of the cave back (mobilized limit) is difficult to predict precisely, it is usually estimated to be rock that has experienced a displacement greater than or equal to 1−2 m (Pierce et al., 2006). However, in this study, the spatial extent of the air gap and mobilized zone (cave zone) are directly mapped into *FLAC3D* from *MassFlow*, where the IMZ growth and material movement are emergent results of the flow model.

2.4.2 Definition of fracture limit

The fracture limit represents the limit between the yielded and seismogenic zones. In this study, the fracture limit is defined based on a back analysis of the deformation induced by caving into the surrounding rock mass at El Teniente mine (Chile) conducted by Cavieres et al. (2003). This study demonstrated that a total strain criterion of 0.5% is a good indicator for delineation of the fracture zone limit from numerical modeling results. This criterion has been used extensively and has been validated further through back analysis of fracture limits at Kiruna (Sainsbury and Stockel, 2012), Grace (Sainsbury and Lorig, 2005), Century Mines (Sainsbury et al., 2016), and Cadia East (Ghazvinian et al., 2020).

The total strain is defined as measure of the principal strain vector:

$$\varepsilon_{tm} = \sqrt{\varepsilon_1^2 + \varepsilon_2^2 + \varepsilon_3^2} \quad (1)$$

3 NUMERICAL MODEL INPUTS

This section describes important components of the numerical model such as in-situ stresses, geotechnical domains, the structural model, and rock mass properties used in this study. In addition, the methodology to simulate the past caves of Lift 1 as broken rock is described.

3.1 In-situ stresses

A re-assessment of overcoring and Sigra measurements conducted by Agapito Associates (2018) at New Afton Mine suggests that the major principal stress is generally trending N-S and dipping sub-horizontally with the minor principal stress assumed as the overburden stress. The horizontal-to-vertical stress ratio for the major principal stress (N-S) is approximately

1.7, while the horizontal-to-vertical stress ratio for the intermediate principal stress (E-W) is 1.1.

3.2 Geotechnical Domains and Structural Model

The geotechnical domains at New Afton have been defined by lithological boundaries. Seven generalized lithology types can be found in the area of the B3 Cave: BXF, Diorite, Monzonite, Picrite, Conglomerate, Kamloops, and Ashcroft. As illustrated in Figure 7, the faults present in New Afton are considered as a geotechnical domain (in red) due to the strong influence on the stability of underground infrastructure, where in some cases its thickness is greater than 30 m. A total of 28 major faults were included in the *FLAC3D* model as a single material of weak rock, i.e., all faults have the same set of material properties. This is an important assumption in the numerical assessment, especially at tunnel-scale where heterogeneity of faulted ground may be more relevant to predict tunnel closure.

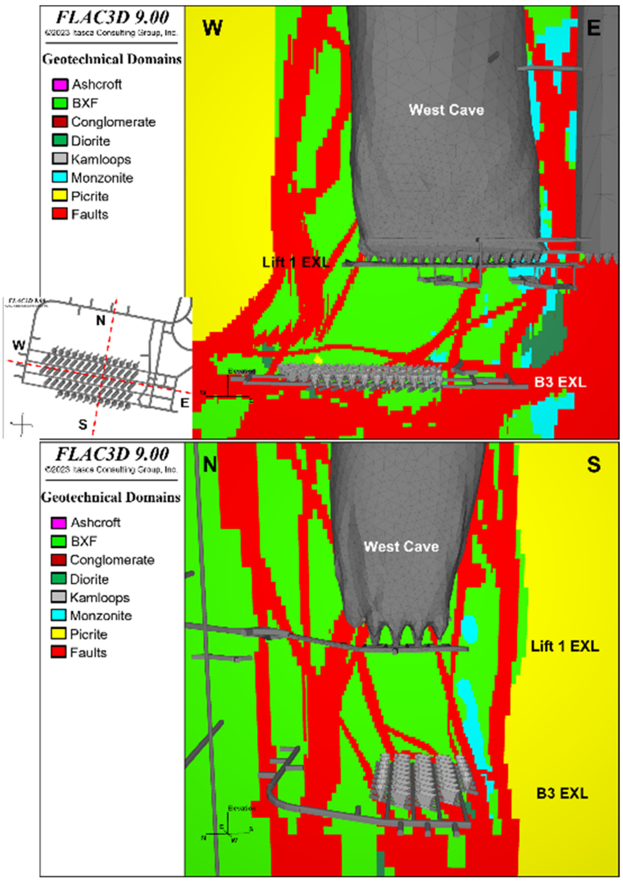

Figure 7 Geotechnical domains along EW and NS cross-sections (up and bottom, respectively).

3.3 Rock Mass Properties

The rock mass characterization was based on laboratory testing and core logging (New Afton, 2016) and previous back-analyses at New Afton Mine. However, during the B3 calibration, fault strength had to be reduced by 50% to match cave-scale observations. The input intact rock properties used and required by *IMASS* are listed in Table 1 (with fault intact UCS already reduced). Note that the intact Young's moduli are scaled to rock mass modulus within *IMASS* using the approach developed by Hoek and Diederichs (2006). The Poisson's ratio is obtained through GSI using the equation developed by Lorig and Varona (2013).

Table 1 Peak strength intact rock properties and geologic strength index (GSI) to derive rock mass properties

Domain	Density (kg/m^3)	GSI	UCSi (MPa)	m_i	E_i (GPa)
Picrite	2700	53	56	15	50
Diorite	2700	45	67	20	36
Conglomerate	2700	44	48	15	24
BXF	2700	60	51	20	45
Kamloops	2700	44	48	15	24
Monzonite	2700	55	62	20	47
Ashcroft	2700	45	67	20	36
Faults	2700	44	24	15	24

3.4 Simulation of pre-existing caves

The simulation of the B3 Cave starts with the pre-existing Lift 1 caves, West Cave (B1), and East Cave (B2), which are initialized as caved material. A single pre-mixed material is assumed to exist within the past caves. As described by Cancino et al. (2022), the caves in Lift 1 exhibited signs of consolidation to an unknown degree due to different factors such as time, lithology, alteration, moisture, and clay content in faulted areas. To investigate B3, both the East and West Caves were initialized with uniform material properties, with their strength determined by averaging the initial lithologies found in the West Cave volume, which is in closer proximity to B3.

The methodology used to initialize the pre-existing cavity is described in detail by Cancino et al. (2022). *FLAC3D* is used to effectively simulate the expected arching behavior inside a cave, and the nonlinear vertical stress variation along the width can be identified. This is achieved by initializing the material inside the past cave as broken rock (to its maximum porosity at an ultimate residual strength in *IMASS*) as well as initializing the stresses to zero, and then letting the broken rock sit under gravity. Consolidation of the caved material is achieved by conducting several cycles of the stress initialization process until a target bulking factor within the cave is reached. Given that estimating the bulking factor within the cave after compaction is very complex, observations of surface subsidence were considered to estimate the number of cycles to conduct the initialization process until matching the fracture limit on surface with the location of mapped tension cracks as depicted in Figure 8.

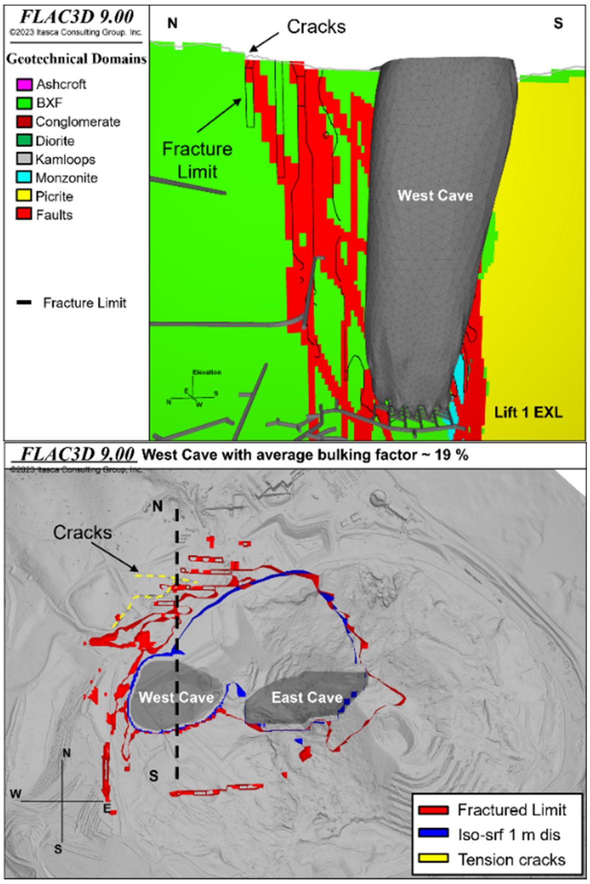

Figure 8 Comparison of fracture limit and cracks on surface after several cycles of initialization of past caves.

3.5 B3 design and production plan

Figure 9 illustrates a plan-view of the B3 production level. The B3 footprint considers four main production drifts (with a spacing of 27 m) with a total of 106 drawpoints (drawbell drifts spaced 16.5 m). Note that half-drawbells are designed for the lateral drifts (I and L) to push abutment stresses away from the perimeter production drifts. The direction of planned undercutting is sequenced from west to east.

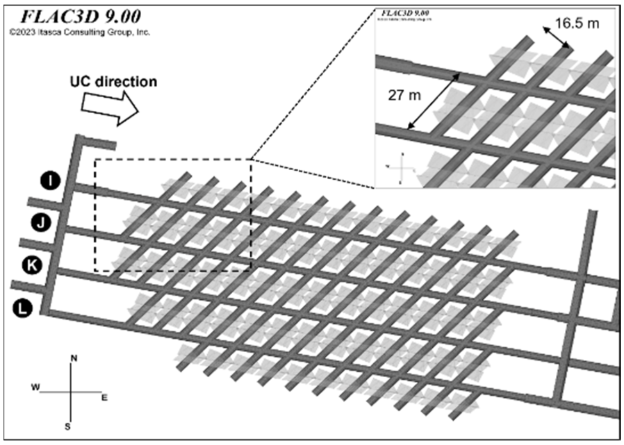

Figure 9 Plan view of the B3 production level.

Figure 10 depicts the draw plan for the B3 Cave, which has been reconciled until May 2023. A total of 51 months of production are planned for the B3 Cave, with a target of 250 kt per month at maximum capacity. Note that during the calibration process, it was necessary to add the blasted material drawn from the drawbell volumes (~6 kt for a full drawbell and ~3.6 kt for half-drawbells) to the draw schedule. Given the relatively low tonnage of this footprint, the blasted material from the drawbells impacts the cave shapes during the first year of draw.

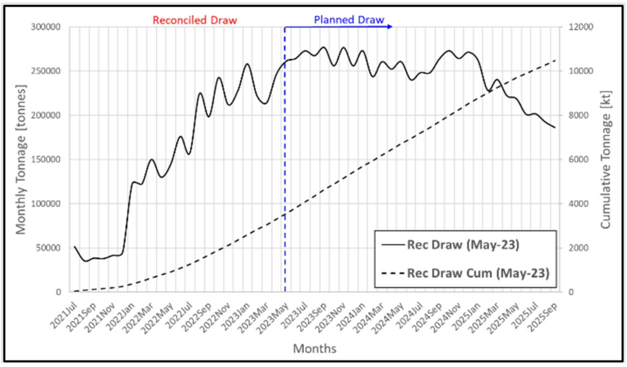

Figure 10 Production plan for the B3 Cave reconciled until May 2023 including the mucked, blasted material from drawbells.

In addition to the draw plan, an advanced undercutting (UC) sequence was implemented explicitly in the model. The UC sequence is implemented by converting the rock volume inside the UC rings to broken rock (at its maximum porosity assumed to be 30% in this study) to simulate blasted material. The upper half of the ring volume is then excavated (nullified in *FLAC3D*) to mimic extraction of blasted material following New Afton mine practices.

3.6 Fragment size and porosity for MassFlow Block Model

The input block model to *MassFlow* was constructed as a subset of the *FLAC3D* model. The important parameters that control bulking, drawdown, and secondary fragmentation are porosity, primary fragment size, and tensile strength. The maximum porosity assumed for all the material was 30% (equivalent to a maximum bulking of 40%), and the initial porosity was set to zero except for the volume of past caves (West and East caves with an initial porosity of 25%).

MassFlow uses a Weibull distribution as input for primary fragmentation. The scale parameter represents the 63rd percentile of the primary fragment size distribution. Given the different materials present at New Afton, different assumptions were made for the scale parameter. Most of the units were assumed to have a scale parameter of 30 cm, except for Picrite and Faults with finer fragmentation (10 cm). In addition, blasted material and past caves were assumed to have a scale parameter of 5 cm. A shape parameter of 3 was assumed for all the materials. Note that no fragmentation assessment was performed in this study (i.e., no calculations for secondary fragmentation or fines migration). However, the primary fragmentation inputs are relevant for development of IMZ within *MassFlow*. The resultant fragmentation curves are illustrated in Figure 11.

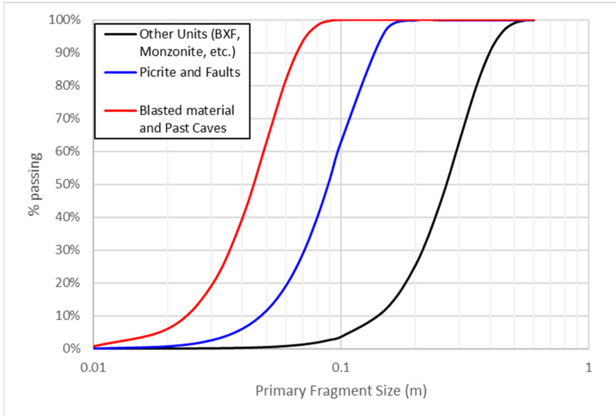

Figure 11 Primary fragmentation assumptions.

4 CALIBRATION OF CAVE PROPAGATION

This section summarizes the results of the back analysis of the B3 Cave. Comparisons between model results and monitoring data (TDR, beacon, Geo4Sight, and published seismic tomography data) are provided.

4.1 Cave Initiation

Figure 12 depicts the predicted cave initiation during January 2022. At this stage, the active drawpoints reached the area covered by the apex level, and the critical hydraulic radius has been met (Kamp et al., 2022). The figure illustrates the initial mobilized zone (yellow markers from *MassFlow* after simulating the drawing for January 2022) and the new mobilized zone at the end of January 2022 (transparent green iso-surface emergent in *FLAC3D*).

The timing of cave initiation observed in the model is well correlated to site observations and the period of January 2022 reported by Kamp et al. (2022) after reaching the critical hydraulic radius (HRcrit), with an increase in seismic response vertically above the cave profile. The estimated HRcrit in the model is ~24 m, which agrees with completion of the apex level area.

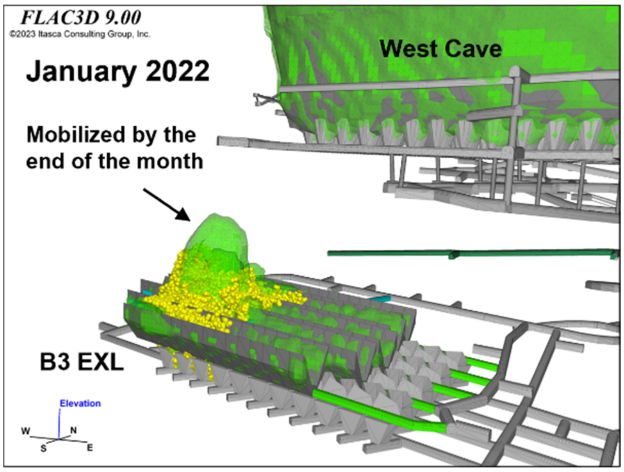

Figure 12 Cave initiation during January 2022 after 7 months of active drawing.

4.2 *Cave Propagation*

The cave propagation was studied in terms of caving rate estimates, TDR breakage timing, comparison with trends of beacon data, Geo4Sight, and with seismic tomography interpretations.

4.2.1 Caving rate estimates

Sainsbury (2012) reported a list of cave propagation rates at numerous operating mines around the world, presenting significant variability in caving rate from 5–31:1, which can be attributed to variations in the in-situ geomechanical conditions, depths, footprint size, and cave mining method employed, many of which were not reported. It is important to note that the caving rates reported by Sainsbury (2012) are based on the ratio of the yield zone height (HoY) to the production draw height measured in solid rock drawn (HoD).

The reconciled draw schedule has been used to determine the HoD for every drawpoint within the B3 cave. The resulting emergent fracture limit within the model is then utilized to approximate the height of the yield zone above each drawpoint in B3. Figure 13 illustrates a whisker plot with the distribution of the estimated caving rates for the active drawpoints for each mining period (month). The caving rate is meaningful for the period between the B3 cave initiation stage through to the B3 fracture limit reaching the Lift 1 fracture limit (between month 6 and 12).

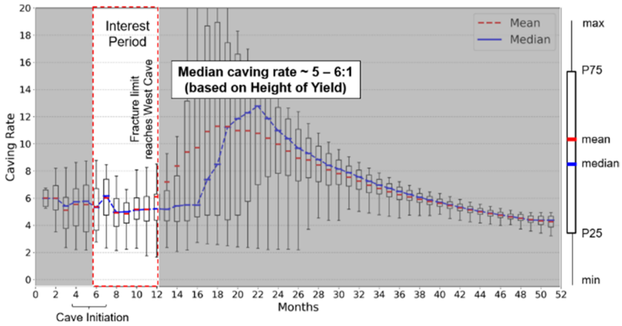

Figure 13 Whisker plot of estimated caving rates based on HoD and HoY.

Following cave initiation, B3 propagates to Lift 1 with a median caving rate ranging between 5:1 and 6:1 (approximately 5:1 when the fracture limit reaches the West Cave). This caving rate is similar to that estimated for the West Cave in Lift 1, with a caving rate ranging between 4:1 and 7:1 at shallower conditions. These results are in line with reported values from Sainsbury (2012) for mines using the panel caving method (5:1 to 10:1).

4.2.2 Comparison with TDR data

TDRs can be beneficial to understand cave behavior as they can provide information on cave initiation, the subsequent progress of the caving zones, and the effect of caving on rock mass fracturing (Szwedzicki et al., 2004; Carlson and Golden, 2008; Kamp et al., 2022).

As mentioned earlier, TDR breakage can be generally expected inside the yielded zone; hence, breakage data can be used to track the evolution of the fracture limit over time. In this study, it is assumed that a fully clipped TDR represents the fracture limit. However, partially clipped TDR data was also used to interpret the behavior of specific TDRs.

For comparison with the numerical model, 17 optical TDRs (OTDR) installed in the B3 ore column were used. These instruments have different lengths and orientation across the B3 column and intersect different geotechnical units.

Figure 14 depicts a comparison between actual TDR UA20-276 breakage data (black line) and the emergent fracture limit from the model (dotted red line) over the life of mine. A good match is observed for this TDR in terms of onset of breakage (early 2022), breakage rate, and timing of complete breakage (November 2022). The UA20-276 is a 160 m long instrument with a plunge of 27° towards the west (contrary to the undercutting direction).

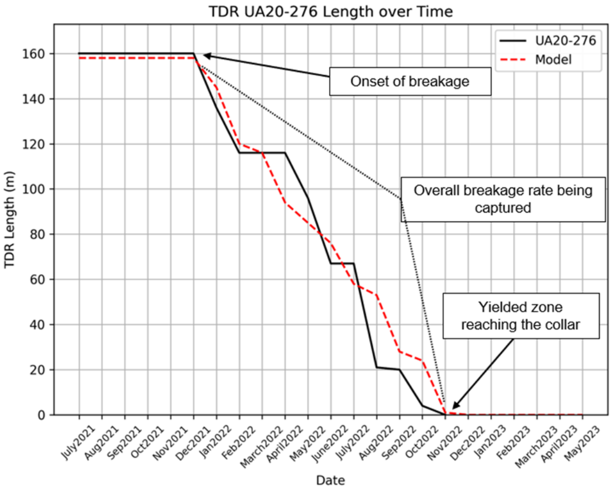

Figure 14 Comparison between TDR UA20-276 breakage data (black line) and the fracture limit (dotted red line) evolution over time.

Figure 15 illustrates an EW cross-section along the TDR UA20-276 location, presenting the geotechnical units, mobilized limit (black line), and fracture limit (blue line) relative to the TDR breakage actual data (red point) for selected periods. The TDR is divided into intact (in white) and broken (in blue) portions over time for easier comparison.

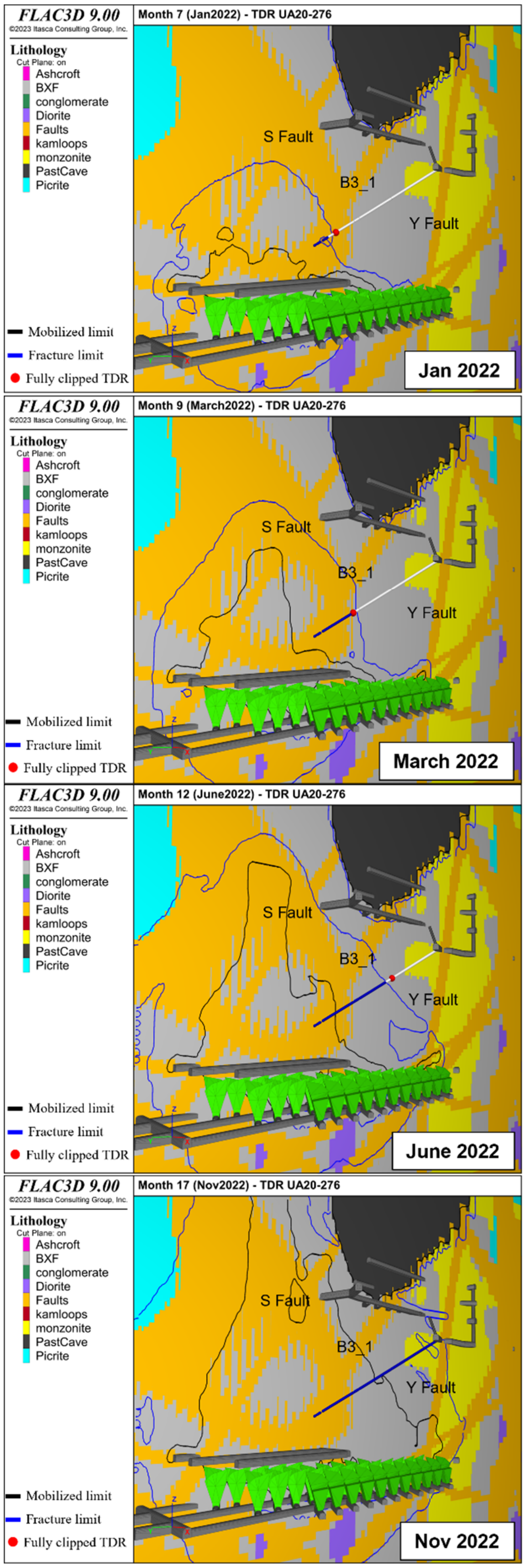

Figure 15 Comparison between TDR UA20-276 breakage data (black line) and the fracture limit (dotted red line) evolution over time.

The same assessment was made for each available TDR to better understand the behavior observed in the model relative to the data. The calibrated model was able to reproduce the trends of most of the TDRs reasonably well (as depicted in Figure 16 for the other four TDRs).

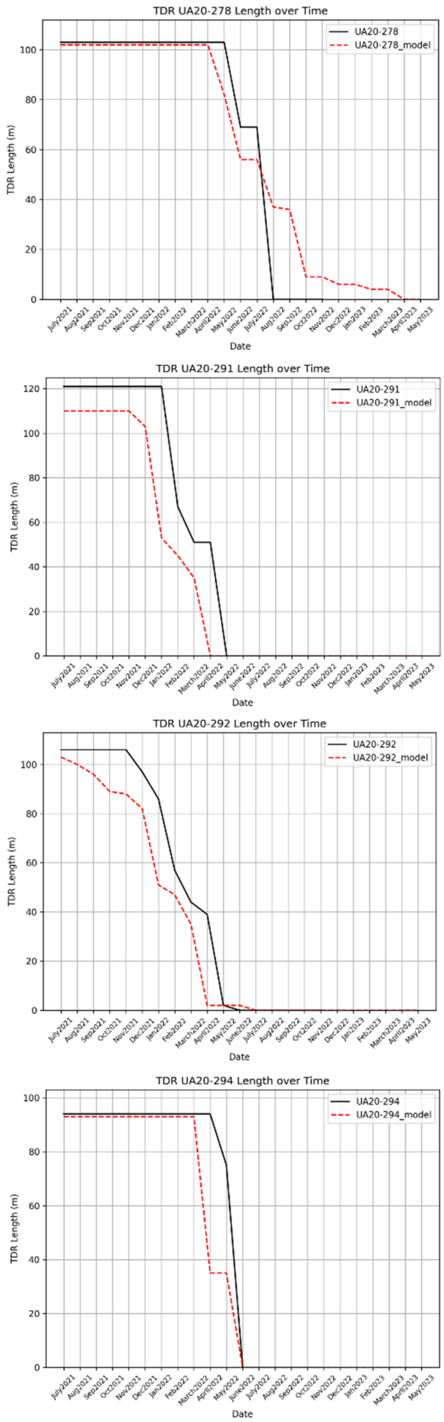

Figure 16 **Comparison between TDR breakage data (black lines) and the fracture limit (dotted red lines) evolution over time for four different TDRs.**

However, the model did not capture well the breakage of short TDRs (11 m long), mainly due to model resolution and TDR location (in faulted ground). Note that in the model, uniform strength properties were assumed for all faults. Strength heterogeneity is likely to exist between faults and even within the same fault, which could lead to different behavior in terms of fracture limit evolution over time.

An example of fault influence is illustrated in Figure 17 for TDRs UA20-288. This TDR, with a length of 130 m, is intersecting the B3_2 fault. Breakage data (Figure 17 left) suggests a major breakage length around July 2022 (black line), while the model suggests an earlier breakage around January 2022 due to the B3_2 fault influence. This difference highlights the importance of correctly capturing in the model the strength heterogeneity associated to this fault.

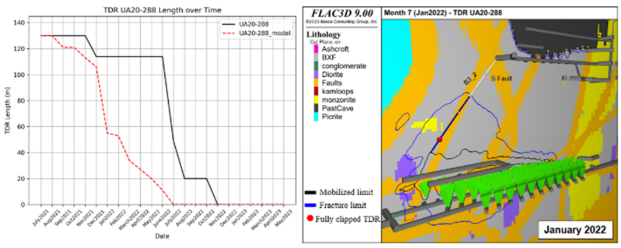

Figure 17 **Left: Comparison between TDR UA20-288 breakage data (black line) and the fracture limit (dotted red line) evolution over time. Right: EW cross-section along the TDR location.**

On the other hand, some faults exhibit reasonable behavior at cave scale as observed for the B3_1 fault. TDR UA20-292 intersects the B3_1 fault, and good correlation is observed between breakage data and fracture limit evolution as depicted in Figure 18. It is important to note that the model demonstrates slightly early onset of breakage, but this TDR exhibited partial breakage in line with model predictions.

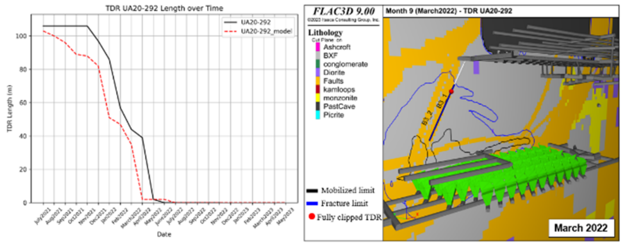

Figure 18 Left: Comparison between TDR UA20-292 breakage data (black line) and the fracture limit (dotted red line) evolution over time. Right: EW cross-section along the TDR location.

4.2.3 Comparison with Beacon data

New Afton has implemented an array of over 90 Elexon Cave Tracker Beacons in the ore column of the B3 Cave to better understand fragmented rock flow within the cave in space and time.

In this study, the beacon movement data is used to compare the growth and shape of the mobilized limit (muck pile).

Confidence of the beacon data is compared against TDR data. Due to intermittent problems and detection issues, reliability of TDR data is believed to be higher than beacon data in this specific case. Beacon trials on site approximate initial movement to commonly exceed a 10-20m range. TDR breakage is used to interpret the beacon data movement, e.g., the beacon movement is disregarded if it moves before the breakage of the TDR in that hole.

Figure 19 illustrates the mobilized limit (in yellow), the beacon movement (grey for the cumulative movement and blue for the movement recorded in the last month), and the location of fully clipped OTDR (in red) for the period between February and April 2022, where the cave grew significantly as indicated by the monitoring system and site observations.

The calibrated model demonstrates overall good agreement between the mobilized limit and the beacon data, capturing the main trends as observed for March and April 2022. It is important to note that some beacons experienced movement before the TDR sensor in the corresponding hole was fully clipped. An example of this is depicted for April 2022 in Figure 19 (bottom). The mobilized limit predicted by the model also does not reach this elevation until July 2022 (see Figure 20), when breakage of the TDR UA20-288 is observed.

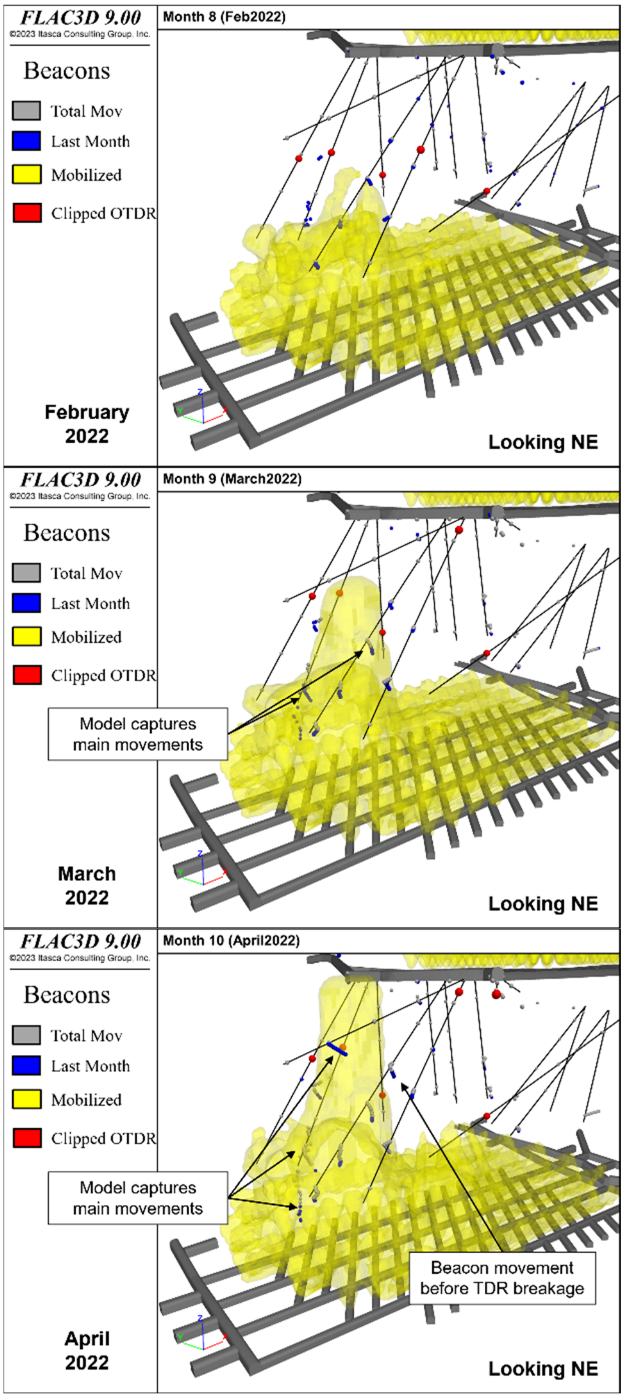

Figure 19 Beacon movement compared to mobilized limit for the period between February and April 2022.

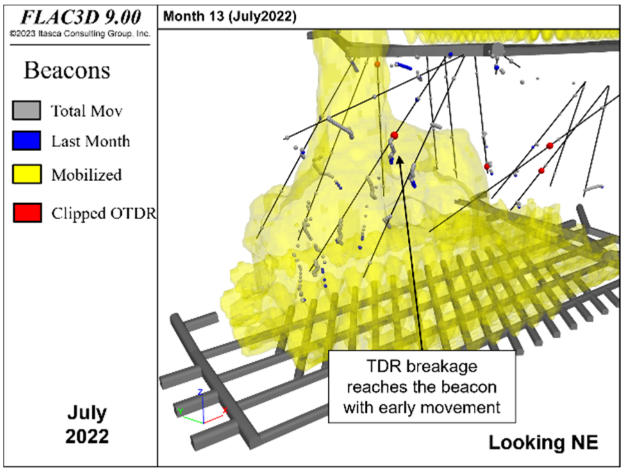

Figure 20 Beacon movement compared to mobilized limit by July 2022.

4.2.4 Comparison with seismic tomography interpretation

Seismic tomography is a technique that helps to interpret relative stress magnitudes and changes over time as mining progresses. It can utilize both mining-induced seismicity (events) and blasts if the seismic waveforms are accurately processed for arrival time and location. Areas of increasing stress exhibit increasing seismic velocities (Vp) since increased stress will result in closing of joints, fractures, microcracks and pore space.

For the first time at New Afton, seismic tomography is being used to help interpret the stress and damage state of the rock mass around the B3 Cave.

Kamp et al. (2022) used the available seismic data to make seismic tomography interpretations of the B3 Cave between September 2021 and March 2022. As depicted in Figure 21, in the pre-caving time frame, before reaching the critical HR (September to December 2021), higher Vp values are observed around the initial undercutting and drawpoint blasting.

During January 2022, after the critical HR was met and the mine production ramped up, an increase in seismic response was observed vertically above the cave profile, growing progressively shallower throughout the month, while the passive tomography data presents a decrease in Vp (stress relaxation/destressing) vertically but an increase in Vp (higher stress) advancing east as the cave front continues to progress.

In the following months (February and March), this trend of increasing Vp values continues for the advancing cave front with a decrease in Vp values (assumed as yielding and cave rock mass) following the vertically growing cave profile. The low Vp values where caving is taking place above the extraction level can be clearly seen in all time periods in Figure 21, aiding with interpretation of the yielding and cave rock mass from mining.

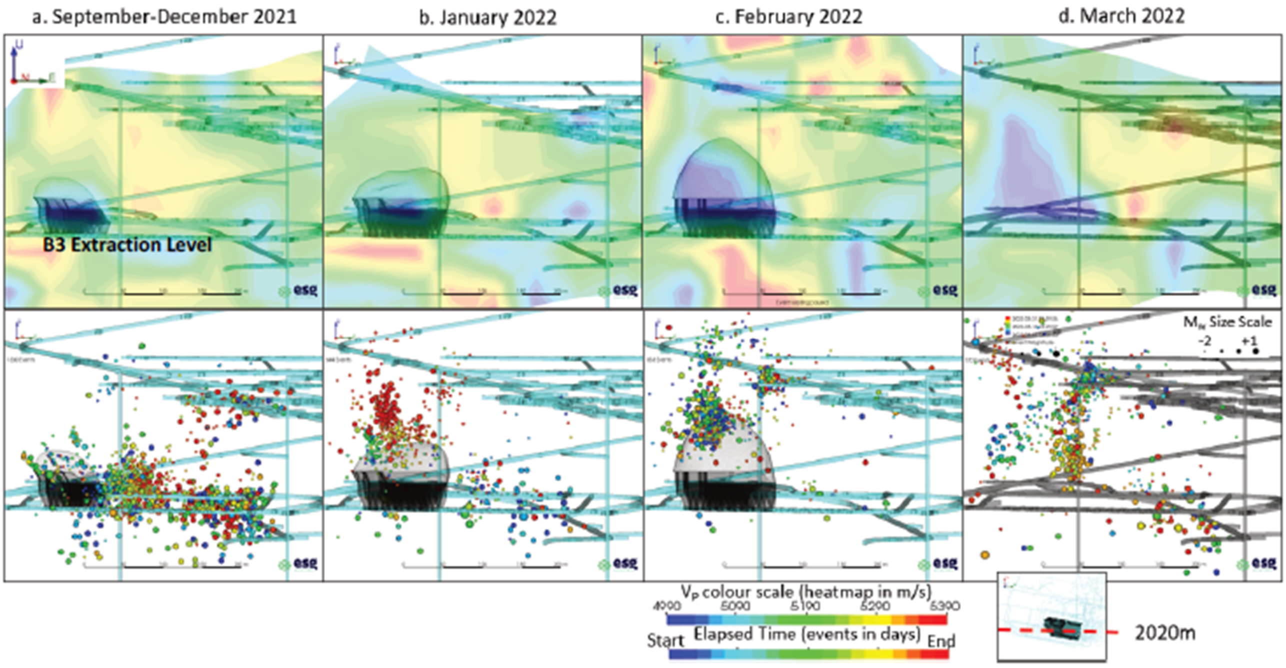

Figure 21 EW cross-section of passive tomography over time (Kamp et al., 2022).

These results are compared to the calibrated *FLAC3D* model in this study. Figure 22 illustrates a similar EW cross-section (N2020) with similar contours of total strain (0.05–3%), mobilized volume (yellow markers), and the interpreted cave back shapes from the mine team using TDR data (in transparent grey). A reasonable correlation between tomography interpretations (Figure 21) and the numerical model trends (Figure 22) are observed in terms of overall rock mass stress/strain conditions based on the expected cave profile. Similar propagation trends over time are observed, with a similar cave shape by March 2022.

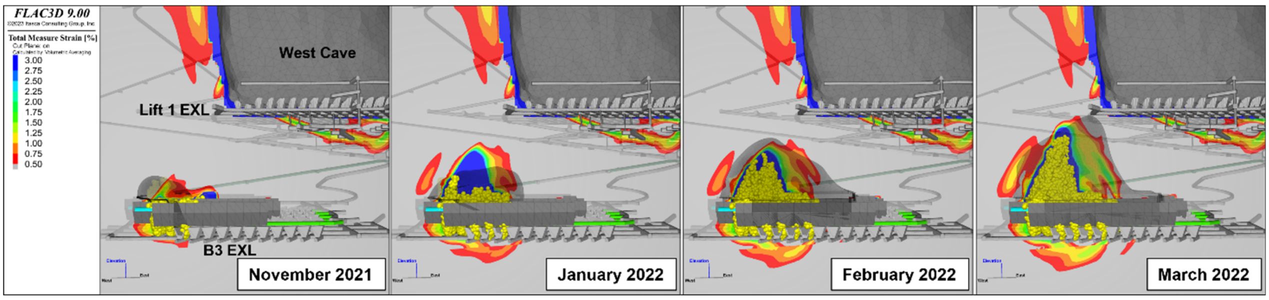

Figure 22 EW cross-section (N2020) of total strain over time in the *FLAC3D* model.

Kamp et al. (2022) reported an example for March 2022 with a low Vp outline interpreted using a Vp threshold of 5090 m/s, and the interpreted cave profile using Elexon Beacons, Elexon Geo4sight, optical and metallic TDR, and March 2022 seismic events.

Figure 23 depicts a comparison between the interpreted shapes (Vp ~5090 m/s in red and monitoring data in blue on top figure) from Kamp et al. (2022) and a similar view of the *FLAC3D* model for the month of March 2022 (bottom). Note that not only the initial mobilized material is presented (in yellow), but also an iso-surface of mobilized zone at the end of the month. This portion of the rock mass is now able to flow if the cave reaches this point in the column. Hence, expected low Vp values are also expected in this area experiencing large deformations. A reasonable match is observed between the interpreted cave shape from seismic tomography (in red on top figure) and the calibrated *FLAC3D* model in terms of mobilized zone (cyan iso-surface on bottom figure) with both reaching the Lift 1 level by March 2022. Some differences are observed towards the west side of the cave due to the orientation (see Figure

17 and Figure 18) and strength of simulated faults. As mentioned in section 4.2.2, the TDR breakage data suggest a higher heterogeneity than simulated for faults. This could also explain the differences between the model and interpreted tomography in the western part of the cave.

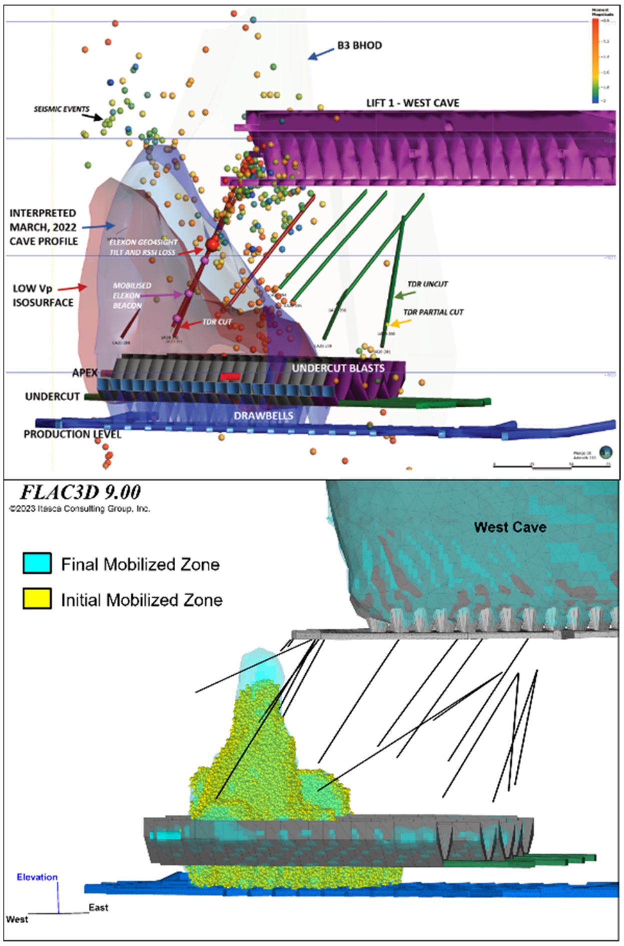

Figure 23 Cave shapes for March 2022. Top: Interpretation of low Vp iso-surface (in red) from Kamp et al. (2022). Bottom: Mobilized limit in the *FLAC3D* model.

5 BREAKTHROUGH PREDICTIONS

5.1 Breakthrough West Cave

Figure 24 illustrates the model predictions for the interaction between the B3 and West Caves. Interaction in terms of fracture limits (cyan iso-surface) is observed during April 2022, and in terms of mobilized limits (yellow iso-surface), early 2023. These results are in line with site observations reported by New Afton after visual inspections in Lift 1 and interpretation of monitoring data (Davenport and Kamp, 2024).

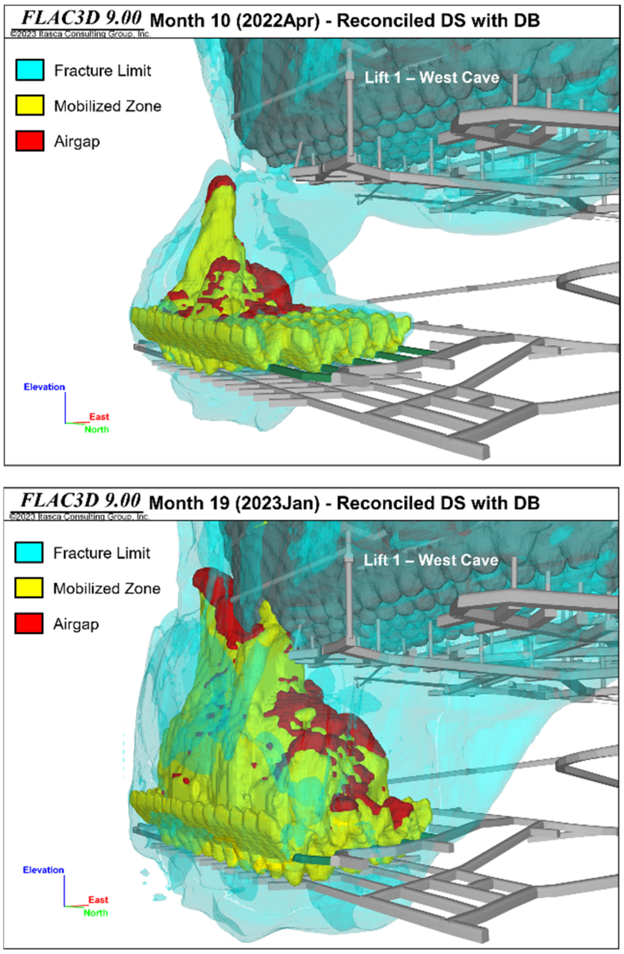

Figure 24 Interaction between B3 and West Caves in terms of fracture (top) and mobilized limits (bottom).

5.2 Breakthrough haulage and vent levels underneath Lift 1

In addition, the model was used to predict the interaction of the B3 Cave with infrastructure underneath Lift 1 to identify areas of serviceability concerns and timing and location of bulkhead installation to delimit safety distances during operation of B3. As depicted in Figure 2, the haulage and vent levels underneath Lift 1 are expected to interact with B3 Cave given its relative location to the B3 footprint.

This interaction is made based on B3 fracture and mobilized limits reaching the haulage and vent levels. Figure 25 illustrates a plan view of the haulage and vent levels with the projected B3 fracture and mobilized limits over time. The B3 fracture limit reaches the haulage level around

August 2022 (after 14 months of active drawing), and the B3 mobilized limit reaches the tunnels around July 2023 (after 25 months of drawing). Figure 25 also depicts the predicted conditions for the end of life of mine (September 2025). By this period, the mobilized limit is predicted to be contained within the boundaries of the B3 production level layout, with a slight extension to the east (upwards in the figure). The fracture limit is also predicted to impact the western haulage and vent levels.

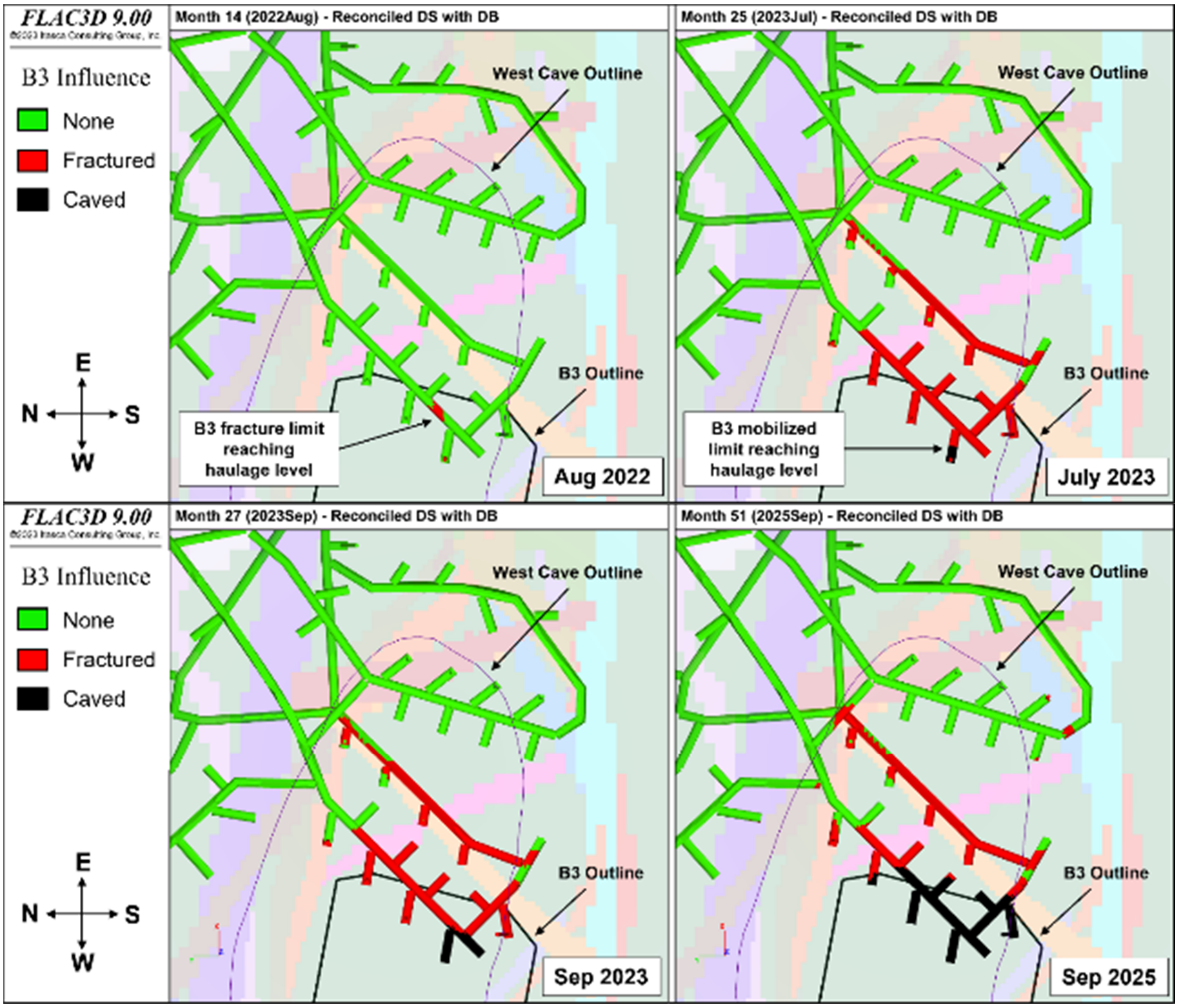

Figure 25 Plan view of the fracture and mobilized limits projected on haulage and vent drifts of Lift 1.

5.3 Breakthrough Lift 1 tunnels

A similar assessment was made for the Lift 1 drifts. Figure 26 illustrates a plan view of the West Cave production level (EXL) with the projected B3 fracture and mobilized limits over time. The B3 fracture limit reaches the West Cave EXL during April 2022, and more significantly during May 2022 (after 11 months of active drawing), and the B3 mobilized limit reaches these tunnels during September 2022. By the end of life of mine, the mobilized limit is predicted to be contained within the projected boundaries of the B3 production level. The fracture limit is predicted to impact all the production drifts limited by the B7_7 fault.

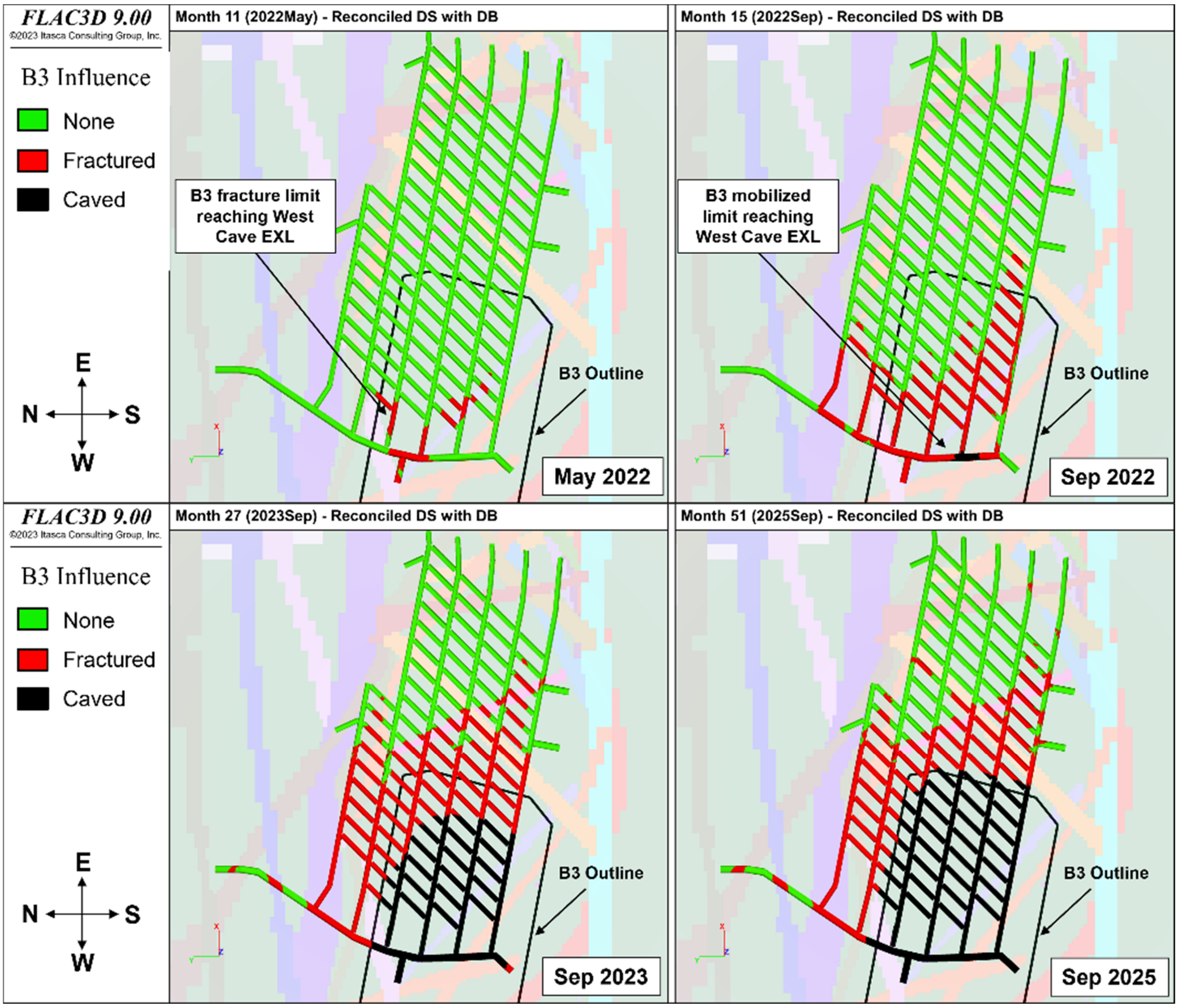

Figure 26 Plan view of the fracture and mobilized limits projected on the West Cave production level.

6 CONCLUSIONS

The hybrid *FLAC3D-MassFlow* approach was used with the *IMASS* model to simulate the caving process at New Afton Mine. Calibration of the B3 Cave was carried out comparing the cave initiation and propagation to TDR breakage data, beacon smart markers movement, and seismic tomography interpretations. An overall good calibration was achieved after many simulations. The fault strength had to be downgraded to match cave-scale observations, which is aligned with the inherent bias on UCS testing for weak material, where the core recovery is usually low and only the best portion of the core is tested. The use of a strain-softening model (*IMASS*) and the hybrid *FLAC3D-MassFlow* approach were key to calibrate the model against different monitoring instruments in terms of fracture and mobilized limits.

In conclusion, considering the complexity of the caving process and geology, rock mass, and fault strength assumptions, the model captures reasonably well the overall TDR breakage evolution when compared to the fracture limit.

A good estimation of the cave shape in terms of mobilized limit is essential for mass balance and air gap formations in the operation. The Cave Tracker System is a valuable monitoring system to improve the understanding of cave flow and calibration of numerical models for further predictions.

The calibrated model was then used to predict the breakthrough timing of the B3 Cave with respect to the mobilized limit of the West Cave, the Lift 1 drifts, and the haulage and vent levels underneath Lift 1. This helped manage the timing of bulkhead installation and definition of safety distances in the active drifts in Lift 1. The calibrated model is also being used to assess the footprint stability of the B3 panel.

ACKNOWLEDGEMENT

The authors wish to thank the management team at New Gold Inc. for approval to publish this work. The New Afton Mine geotechnical team is also acknowledged for their ongoing risk management efforts.

REFERENCES

Agapito Associates Inc. (2018). Determination of horizontal principal stresses using the downhole overcoring method at the New Afton Mine, Kamloops, British Columbia. Technical report prepared for New Gold Inc.

Cancino, C., Fuenzalida, M. & Kamp, C. (2022). Modeling considerations for cave compaction at New Afton Mine, in Y Potvin (ed.), Caving 2022: Fifth International Conference on Block and Sublevel Caving, Australian Centre for Geomechanics, Perth, pp. 573-582, https://doi.org/10.36487/ACG_repo/2205_39.

Carlson, G., & Golden. R. (2008). Initiation, growth, monitoring and management of the 7210 cave at Henderson mine – A case study, 5th International Conference and Exhibition on Mass Mining, MassMin 2008, Luleå, Sweden.

Cavieres, P., Gaete, S., Lorig, L. & Gómez, P. (2003). Three-Dimensional Analysis of Fracturing Limits Induced by Large Scale Underground Mining at El Teniente Mine, in Soil and Rock America 2003 (39th U.S. Rock Mechanics Symposium, Cambridge, Massachusetts, June 2003), 893–900, P. J. Culligan, H. H. Einstein, and A. J. Whittle, Eds. Essen: Verlag Glückauf.

Davenport, K. & Kamp, C. (2024). Influence of pre-existing mobilized zones on B3 Cave propagation and initial subsidence at the New Afton Mine, in Proceedings of the Nineth International Conference and Exhibition on Mass Mining (MassMin 2024, September), Kiruna.

Duplancic, P. & Brady, B. H. (1999). Characterization of caving mechanisms by analysis of seismicity and rock stress, in Proceedings of the 9th ISRM Congress on Rock Mechanics, Vol 2., pp. 1149-1053, Paris, France.

Fuenzalida, M., Pierce M. & Katsaga, T. (2018). REBOP-FLAC3D hybrid approach to cave modelling, in Proceedings of the Fourth International Symposium on Block and Sublevel Caving (Vancouver, Canada 2018), Y Potvin & J Jakubec (eds), pp. 297-312. Perth: Australian Centre for Geomechanics.

Ghazvinian, E., Fuenzalida, M., Orrego, C. & Pierce, M. (2020). Back analysis of cave propagation and subsidence at Cadia East Mine, in Proceedings of the Eight International Conference and Exhibition on Mass Mining (MassMin 2020, December), Santiago: University of Chile.

Ghazvinian, E., Garza-Cruz, T., Bouzeran, L., Fuenzalida, M., Cheng, Z., Cancino, C. & Pierce, M. (2020). Theory and Implementation of the Itasca Constitutive Model for Advanced Strain Softening (IMASS), 8th International Conference & Exhibition on Mass Mining, MassMin 2020, 451–461. Santiago: University of Chile.

Hoek, E., & Diederichs, M. S. (2006). Empirical Estimation of Rock Mass Modulus, in *Int. J Rock Mech. Min. Sci.*, 43, 203–215.

Itasca Consulting Group, Inc. (2019). REBOP — Rapid Emulator based on Particle Flow Code (Version 4.0). Minneapolis: Itasca.

Itasca Consulting Group, Inc. (2023a). FLAC3D — Fast Lagrangian Analysis of Continua in Three Dimensions (Version 9.0). Minneapolis: Itasca.

Itasca Consulting Group, Inc. (2023b). MassFlow — A gravity flow simulator (Version 9.0). Minneapolis: Itasca.

Kamp, C., Conley, A., Collins, D. S., Preiksaitis, M., Butler T. & Shumila, V. (2022). Use of seismic tomography to aid rock mechanics interpretation at New Afton B3 block cave mine, in Y Potvin (ed.), Caving 2022: Fifth International Conference on Block and Sublevel Caving, Australian Centre for Geomechanics, Perth, pp. 461-472, https://doi.org/10.36487/ACG_repo/2205_31.

Lorig, L. & Varona, P. (2013). Guidelines for numerical modeling of rock support for mines, in Proceedings of the 7th International Symposium on Ground Support in Mining and Underground Construction, E. Potvin and B. Brady (eds), Perth, pp. 81-105.

Lupo, J. F. (1998). Large-scale surface disturbances resulting from underground mass mining, *Int. J. Rock Mech. Min. Sci.*, *35*(4-5), Paper No. 25.

New Afton Mine (2016). Section 6, Rock Properties., Technical Report MIN-PLAN S204, GCMP.

Pierce, M., Cundall, P., Mas Ivars, D., Darcel, C., Young, R. P., Reyes-Montes, J. & Pettitt, W. (2006). Mass Mining Technology Project: Six Monthly Technical Report, Caving Mechanics, Sub-Project No. 4.2: Research and Methodology Improvement, and Sub-Project 4.3, Case Study Application, ICG06-2292-1-Tasks 2-3-14, Itasca Consulting Group Inc.

Pierce, M. (2010). A Model for Gravity Flow of Fragmented Rock in Block Caving Mines. Ph.D. Thesis, University of Queensland, Brisbane.

Pierce, M. E. (2013). Numerical Modeling of Rock Mass Weakening, Bulking and Softening Associated with Cave Mining, ARMA e-Newsletter Spring 2013, 9.

Sainsbury, D. & Lorig, L. (2005). Investigation of Mining-Induced Subsidence at the Abandoned Grace Mine, ITASCA Minneapolis, Report to New Morgan Properties, L.P., Ref. ICG04-2262-29.

Sainsbury, B. (2012). A model for cave propagation and subsidence assessment in jointed rock masses. Ph.D. Thesis, University of South Wales.

Sainsbury, B. & Stockel, B. M. (2012). Large-scale caving and subsidence assessment at the Kiirunavaara Lake Orebody, In Proceedings, 6th International Conference & Exhibition on Mass Mining (MassMin 2012, Sudbury, Canada, June 2012), pp 243–253. Canadian Institute of Mining, Metallurgy and Petroleum: Montreal.

Sainsbury, D. P., Sainsbury, B. L. & Sweeney, E. (2016). Three-dimensional analysis of complex anisotropic slope instability at MMG's Century Mine,. *Mining Technology*, *125*(4), 212–225.

Szwedzicki, T., Widijanto, E. & Sinaga, F. (2004). Propagation of a caving zone, a case study from PT Freeport, Indonesia, in 4th International Conference & Exhibition on Mass Mining, MassMin 2004, 508–512. Santiago.